Investigations of semiconductor surfaces and interfaces by X-ray grazing incidence diffraction

Ullrich Pietsch

Institut fuer Physik, Universitaet Potsdam, D-14415, Potsdam, Germany

Non-coplanar X-ray grazing incidence diffraction is an appropriate method to investigate the strain and compositional set-up of semiconductor nanostructures. Exploiting refraction effects at the air–sample interface, the penetration depth of the probing X-ray can by tailored between a few and several hundred nanometers below the surface. While the detected signal is Bragg-diffracted at a lattice plane directed perpendicular to the surface, the method possesses the capability for a depth-resolved analysis of the relaxation state in semiconductor multilayers. Beside vertically stacked structures, it can be applied for the investigation of laterally patterned nanostructures, such as free-standing and buried surface gratings. This article will introduce the reader to the experimental set-up, the resolution condition, and theoretical approaches necessary for running and interpreting GID-experiments, followed by a brief review of recent applications.

1. Introduction

The development in semiconductor technology is currently characterized by a downscaling of the dimension of active elements. In order to exploit quantum effects, the thickness of the active layer has to be of the order of the excitonic radius of the respective material; for GaAs this is 10 nm. The limitation of the vertical layer thickness down to several manolayers, single quantum wells (SQW), creates atomic-like energetic levels above the conduction and below the valence band of the active material which modifies the electronic band gap. This opens the opportunity for tailoring the photoluminescence energy by controlled preparation[1].

Additional lateral patterning (quantum wires, QW) increases the density of states close to the quantization levels, gives rise to an increase in the efficiency of radiative recombination, and lowers the threshold of the respective laser devices. Patterning in both lateral directions (quantum dots, QD) creates 3D atomic aggregates on a mesoscopic level which provides new physical properties[2].

e-mail: upietsch@ullipc.physik.uni-potsdam.de

The technological process of nanostructure preparation requires non-destructive methods for sample characterization. Whereas scanning-probe techniques are used to characterize film surfaces, X-ray techniques still remain important for probing the internal interfaces and the vertical and lateral correlation of mono- and multilayer structures near the sample surface[3]. Beside their non-destructiveness, the refraction of the X-ray beam at the air–sample interface makes the techniques most sensitive for thin-layer analysis. Since the refractive index of matter for X-rays is smaller than unity, the X-ray penetration depth can be drastically reduced to several nanometers if the beam strikes the sample surface at a very shallow grazing angle. Thus the vertical density profile can be probed by X-ray specular reflectometry. In the wide-angle region, conventional coplanar X-ray diffraction techniques have been improved in order to enhance the sensitivity with respect to small strain fields and lattice mismatches. Extreme near-surface sensitivity could be realized by the use of strong-asymmetric diffraction schemes[4,5] and, in particular, by the X-ray grazing incidence diffraction (GID) method, which combines the depth sensitivity of X-ray reflection and the strain sensitivity of the wide-angle X-ray diffraction.

The GID technique was first applied by Marra *et al.*[6] to identify a very thin gold layer on GaAs. Their experimental scheme is based on a paper published by Vineyard[7] which first investigated the consequences of a shallow angle of incidence on the diffraction intensity in terms of the first-order Born approximation. Dosch *et al.*[8] have shown that this approach is inappropriate. They published experimental evidence that the scattering intensity in this scheme is mainly controlled by the Fresnel transmission function and that the structure factor peaks at the critical angle of total external reflection α_c. This behaviour can be entirely understood in terms of the distorted-wave Born approximation (DWBA)[9].

Early applications of the GID scheme in Western Europe are based on this approach. Dosch and his group have used this technique for the investigation of near surface structural phase transitions in metallic systems[10]. Bernhard *et al.*[11] and Rugel *et al.*[12] have studied the surface damage of ion-implanted silicon.

Independent from the above-mentioned development, a dynamical theory of GID was introduced by Afanasev and Melkonyan[13] which initiated a new line of surface-sensitive experiments at the Institute of Crystallography in Moscow in the mid-eighties. Publications emerged investigating the near surface region of silicon surfaces using GID[14,15].

The first application of GID on semiconductor multilayers has been published in the early nineties[16] where it was demonstrated that different sublayers can be probed step-by-step by changing the angle of incidence, α_i from $\alpha_i < \alpha_c$ to $\alpha_i > \alpha_c$. This will be explained in more detail in the following sections.

2. Refraction and diffraction

X-ray scattering is well-described in terms of reciprocal space. Using the scattering scheme introduced in Figure 1 the reciprocal space co-ordinates are

$$Q_x = K(\cos\alpha_f \cos\theta_f - \cos\alpha_i \cos\theta_i), \quad (1)$$

$$Q_y = K(\cos\alpha_f \sin\theta_f + \cos\alpha_i \sin\theta_i), \quad (2)$$

$$Q_z = K(\sin\alpha_f + \sin\alpha_i). \quad (3)$$

α_i and α_f are the incidence and exit angles with respect to the surface; θ_i and θ_f are the angles measured with respect to in-plane vector Q_x as demonstrated in Figure 1. $K = |K_0| = |K_L|$ is $2\pi/\lambda$, λ being the wavelength. Assuming $\theta_i = \theta_f = 0$ and $\alpha_i = \alpha_f$ the scattering takes place within the (Q_x, Q_z) plane only and the z-components of the electric field vectors are $E_0 e^{(iQ_z z)}$ and $E_r e^{(iQ_z z)}$.

While the refractive index outside the sample is unity, its value inside is

$$n = 1 - \frac{1}{2}(\chi'_0 + i\chi''_0) = 1 - \frac{\lambda^2 r_e}{2\pi}\rho + i\frac{\mu\lambda}{4\pi}. \quad (4)$$

Here χ'_0 and χ''_0 are the real and imaginary parts of the dielectric susceptibility at the origin of reciprocal space which are connected with the electron density ρ and the X-ray absorption coefficient μ of the material, respectively; r_e is the 'electronic radius'. Due to the fact that $\chi_0 <> 0$ the z-component of the field vector within the sample (Q_z in eq. (1)) has to be replaced by

$$q_z = K\left[\sqrt{\sin\alpha_f^2 - \sin\alpha_c^2} + \sqrt{\sin\alpha_i^2 - \sin\alpha_c^2}\right], \quad (5)$$

this z-component becomes $E_t e^{(iq_z z)}$, where E_t is the transmitted electric field vector. In the following we consider the reciprocal space inside and outside the sample.

For small $\alpha_{i,f}$ the Fresnel coefficients of reflection r and transmission t are

$$r = \frac{\alpha_i - \sqrt{\alpha_i^2 - \alpha_c^2}}{\alpha_i + \sqrt{\alpha_i^2 - \alpha_c^2}}, \quad (6)$$

$$t = \frac{2\alpha_i}{\alpha_i + \sqrt{\alpha_i^2 - \alpha_c^2}}, \quad (7)$$

using the relation

$$\alpha_c = \sqrt{\chi_0}. \quad (8)$$

If $\alpha_i < \alpha_c$ the incoming wave becomes evanescent and propagates in the (q_x, q_y) plane. Its penetration depth Λ towards the sample is non-zero. It is of the order of the decay length of the transmitted wave into the sample, given by the reciprocal of the imaginary part of q_z shown in eq. (5),

$$\Lambda = \frac{1}{\mathrm{Im}\, q_z}. \quad (9)$$

Λ is proporational to $1/\sqrt{\alpha_c^2 - \alpha_{i,f}^2}$ if $\alpha_{i,f} < \alpha_c$ and $\alpha_{i,f}/\mu$ if $\alpha_{i,f} >> \alpha_c$. The functional behaviour of Λ versus α_i is shown in Figure 2. For GaAs the minimum Λ is about 5 nm. Depending on the ratio between α_i and α_f the penetration depth approaches about 300 nm for grazing angles of about 1° using copper radiation.

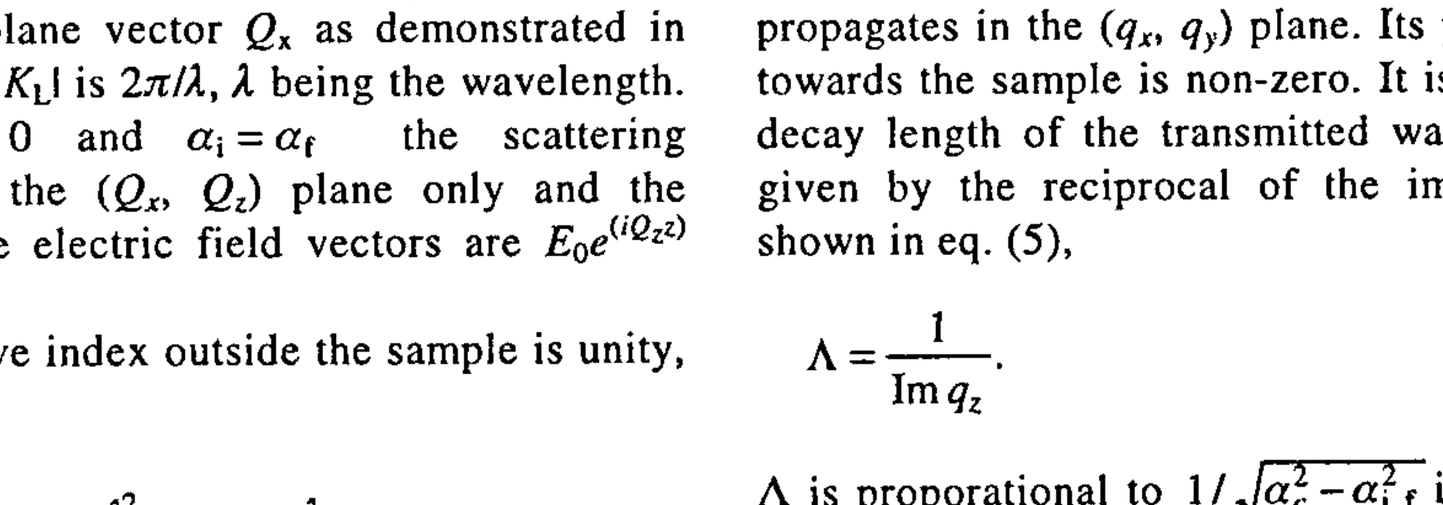

Figure 1. Definition of angles and directions of the GID set-up.

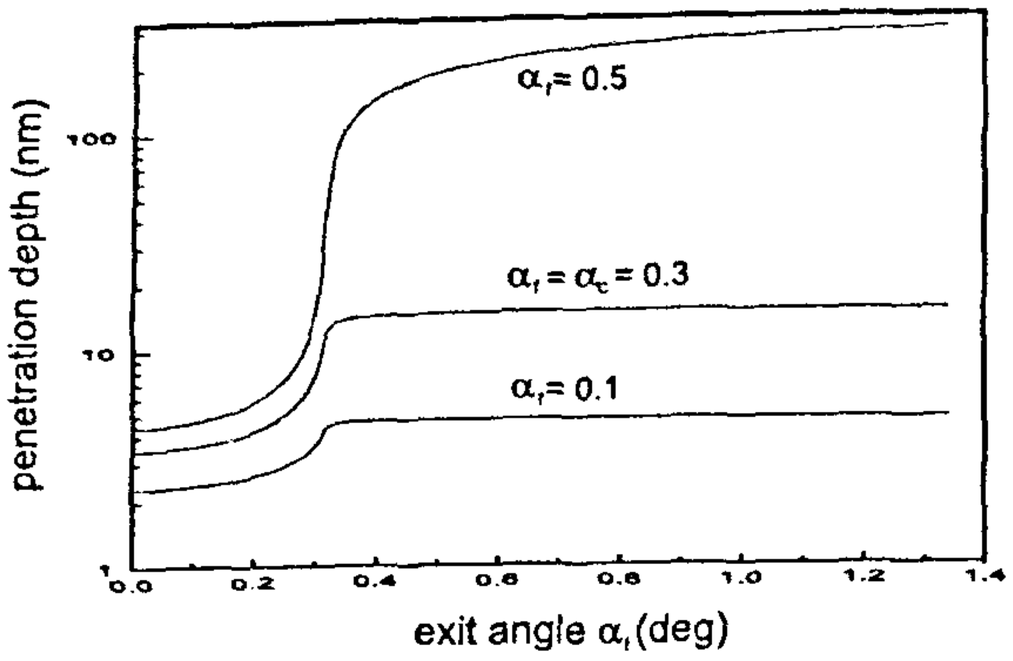

Figure 2. Effective penetration depth below a GaAs surface for a *GID experiment, calculated for different angles* of incidence and exit.

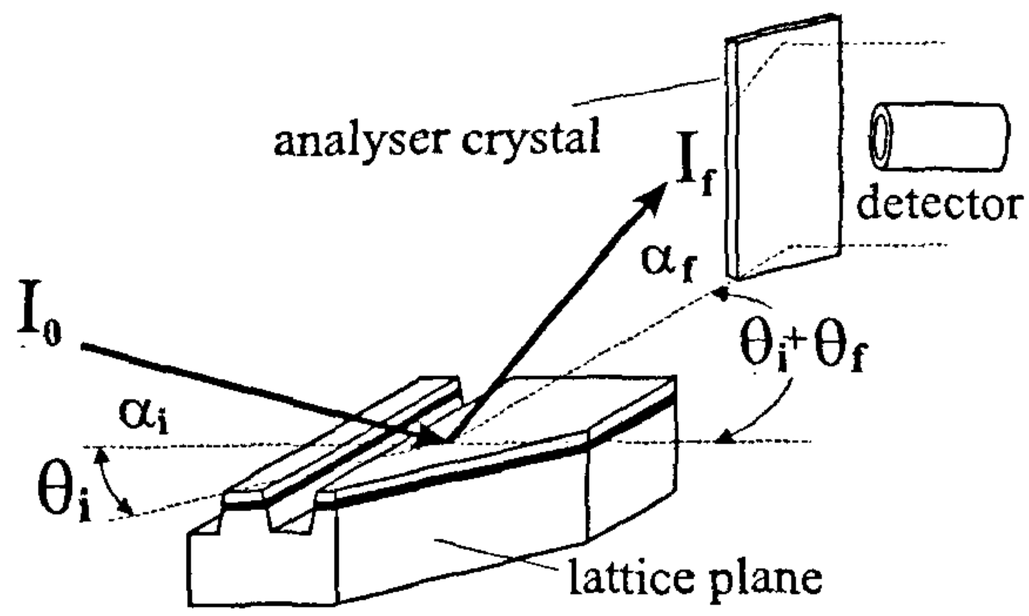

Figure 3. Schematic set-up of the grazing incidence experiment for the particular case of inspecting patterned surfaces.

Rotating the sample about the surface normal, any Bragg diffraction peak may appear if the in-plane angles $\theta_i \approx \theta_f$ (see Figure 1) are close to the respective Bragg angle θ_B. Then a reflected and additionally Bragg-diffracted wave propagates in the k_H direction. The intensity of this wave depends on the deposited energy below the sample surface, i.e. the magnitude of the transmission function $t(\alpha_{i,f})$. For fixed α_i the reflected–diffracted wave reaches a maximum if α_f equals α_c.

Due to the truncation of 3D space by the sample surface, the intensity distribution of a Bragg diffraction peak is no longer a single point in reciprocal space. The Bragg intensity is smeared out in a direction perpendicular to the surface. These so-called truncation rods contain the complete information about the electron density variation along the sample normal.

3. Experimental realization

The experimental set-up is shown in Figure 3. A well-collimated monochromatic incident beam strikes the sample surface at α_i. The specularly reflected beam can be detected at an exit angle $\alpha_f = \alpha_i$. Maximum in-plane intensity is expected whenever any in-plane Bragg condition is satisfied. At this angular position the variation of the reflected–diffracted beam can be recorded as a function of α_i. Its intensity maximum can be used to calibrate the critical angle α_c which is necessary to calibrate the angular coordinates of the diffractometer with the reciprocal space coordinates of the sample.

The intensity distribution is recorded usually across any direction within the (q_x, q_y) plane (in-plane scans) or as a function of q_z for fixed $q_{x,y}$ (truncation rod scans). Using a position-sensitive detector (PSD) the reciprocal space is inspected on a circle slightly inclined with respect to q_z.

The three coordinates of the reciprocal space can be varied by changing four angles α_i, α_f, θ_i and θ_f. Thus there is the opportunity to vary the reciprocal space coordinates without losing the depth resolution. In most cases α_i was kept fixed and the other three angles were used for scanning the reciprocal space.

The resolution in reciprocal space depends on geometric restrictions in the experiment. Because the intensity of the reflected–diffracted wave is of the order of only 10^{-8}, efficient GID experiments require high-power X-ray sources, such as synchrotron radiation. They provide high-intensity and a *well-collimated incident beam* which can be tuned over a wide range of wavelengths. The experiment can be equipped with optical elements *which improve the resolution, such as* double-crystal monochromators before and an analyser crystal behind the sample. The detection of truncation rods is performed by scanning at least two of the four angles. The variation of the other two follows from the conditions

$$\cos\alpha_f \cos\theta_f = \cos\alpha_i \cos\theta_i, \tag{10}$$

$$\cos\alpha_f \sin\theta_f + \cos\alpha_i \sin\theta_i = 2\sin\Theta_{B\|}, \tag{11}$$

where $\Theta_{B\|}$ is the lateral projection of the Bragg angle.

Now we introduce an azimuthal deviation $\eta_{i,f} = \theta_{i,f} - \Theta_{B\|}$. Assuming $|\alpha_{i,f}| << 1$ and $|\eta| << 1$ we obtain the direction angles of the diffracted beam using the *master formula* of GID[17,18].

$$\eta_{i,f} = \frac{1}{2}\alpha_{i,f}^2 \sin(2\Theta_{B\|}) - \eta_{i,f}\cos(2\Theta_{B\|}),$$
$$\alpha_{f,i}^2 = \alpha_{i,f}^2 \cos(2\Theta_{B\|}) + 2\eta_{i,f}\sin(2\Theta_{B\|}). \tag{12}$$

As a consequence any divergence $\Delta\eta_i$ of the incident beam in the azimuthal direction with no divergence in the vertical direction ($\Delta\alpha_i \approx 0$) initiates an azimuthal divergence of the diffracted beam

$$\Delta\eta_f = \Delta\eta_i \cos(2\Theta_{B\parallel}), \tag{13}$$

and a vertical divergence as well,

$$\Delta\alpha_f = \frac{\Delta\eta_i}{\alpha_f} \sin(2\Theta_{B\parallel}). \tag{14}$$

On the other hand, the simultaneous excitation of the entire truncation rod for fixed α_i requires a non-vanishing in-plane divergence $\eta_{i,f}$. The smaller η_i, the shorter the illuminated part of the truncation rod. The results for both fixed α_i and fixed α_f can be summarized by the condition

$$\alpha_{i,f}\Delta\alpha_{f,i} = \eta_{f,i} \sin 2\theta_{B\parallel}. \tag{15}$$

The validity of these relations has been confirmed experimentally[19].

4. Theoretical description

An extension of the GID dynamical theory on multilayers was first presented by Rhan and Pietsch[20]. After this a complete GID dynamical theory has been developed by Stepanov *et al.*[21]. It is based on a matrix approach and is available via the internet[22]. It is valid in general, but only a few highly-perfect materials require its application. An application of the dynamical approach for laterally mismatched heterosystems has been proposed by Ulyanenkov *et al.*[23].

Many interesting material systems can be interpreted in terms of a semi-kinematic approach based on DWBA. Expressed in terms of the reciprocal space coordinates of the sample, the GID intensity is the square of the scattering amplitude $A(q_x, q_z)$[24]

$$I(q_x, q_z) = [t(\alpha_i)t(\alpha_f)A(q_x, q_z)]^2 \exp(-\sigma^2 q_z^2), \tag{16}$$

corrected by the transmission functions with respect to the angles of incidence and exit which treat the refraction of the X-ray wave at the air–sample interface. In most cases the density differences between the sublayers of the sample are so small that the multiple scattering between the internal interfaces can be neglected. Then $t(\alpha_{i,f})$ is described by eq. (7) using an average sample density. To do that, $\langle\chi_0\rangle$ is averaged across the respective penetration depth

$$\langle\chi_0\rangle = \int_0^\Lambda dz \chi_0(z). \tag{17}$$

The Gaussian in eq. (16) is an overall damping function containing σ as a parameter which represents the average surface and interface roughnesses for the sample. At the particular in-plane scattering vector, **H** the scattering amplitude $A(q_x, q_z)$ is expressed by

$$A(q_x, q_z) = \sum_{n=1}^{N} A_n'(q_x)\chi_{H,n} \frac{e^{iq_z z_{n-1}} - e^{iq_z z_n}}{1 - e^{iq_z a_0}}, \tag{18}$$

where z_n are the sublayer distances in the z-direction measured from the top of the sample down to the bulk; α_0 is the in-plane lattice parameter of the substrate; $\chi_{H,n}$ are the respective Fourier components of the dielectric susceptibility. $A'(q_x)$ contains the in-plane variation of the electron density. If the surface is non-patterned, it is simply the resolution function for the experiment. For a lateral grating $A'(q_x)$ is expressed by[25,26],

$$A'(q_x) = |f(q_x, q_z)| \sum_j \delta\left(q_x - j\frac{2\pi}{D}\right), \tag{19}$$

$$\text{with } f(q_x, q_z) = \frac{1}{iq_z} \int_{D/2}^{D/2} e^{i(q_x x + q_z z(q_x))}. \tag{20}$$

The sum in eq. (19) describes the lateral correlation function of the one-dimensional grating with periodicity D. δ is the in-plane resolution function which becomes the Kronecker-δ whenever the lateral correlation goes to infinity. $f(q_x, q_z)$ is the grating shape function (note the q_z dependence).

The simulation problem consists of finding the correct layer thicknesses $t_n = z_{n-1} - z_n$ and the respective susceptibilities $\chi_{H,n}$ of the sublayers as well as the determination of the lateral shape function (for gratings). For the fitting procedure it is helpful if the sample can be inspected at different depths Λ below the surface and that the respective scattering curves match a unique set of fit parameters.

Recording a rod scan at the in-plane scattering vector **H** of the substrate, the strength of scattering of individual sublayers is a measure of the pseudomorphy of the heterostructure. The scattering strength is a maximum, i.e. $\chi_H = \chi_{H,max}$ for lattice matched heterostructures and $\chi_H = 0$ for a completely relaxed sublayer. Depending on the deviation from the in-plane Bragg condition, it may vary in the range $0 < \chi_H < \chi_{H,max}$. Also, for amorphous layers χ_H is zero. This may happen right close to the surface[12,15] or after ion implantation in a buried layer[27].

5. Applications

5.1. *Measuring layer thicknesses*

The GID technique is very sensitive to thin layers close to the surface. To apply this technique for measuring the

layer thickness t, the truncation rod has to be inspected close to the angular position of an in-plane Bragg peak excited at Θ_{Bll} and using a fixed angle of incidence $\alpha_i > \alpha_c$. Under this condition, the vertical momentum transfer is only varied by changing α_f. In reciprocal and angular space and for $\alpha_f >> \alpha_c$, it yields

$$t = \frac{2\pi}{\Delta q_z} \approx \frac{\lambda}{\alpha_{f,m+1} - \alpha_{f,m}}. \quad (21)$$

This is demonstrated in Figure 4. It shows the intensity distribution of (200) in-plane diffraction from a (001) oriented GaAs/InAs/GaAs double heterostructure as a function of α_f, recorded for different values of α_i. Independent of α_i, one sharp peak first appears at $\alpha_f = \alpha_c$. It reflects the maximum of the Fresnel transmission function (see eq. (7)). For $\alpha_i < \alpha_c$ no additional peak appears, because the penetration depth is smaller than the top layer thickness (see Figure 2). On increasing α_i, Λ increases and the X-ray beam gets scattered at the intrinsic interfaces of the sample. Thus several thickness oscillations appear for $\alpha_f > \alpha_c$.

From eq. (21), the top layer thickness is obtained as $t_{top} = 37 \pm 1$ nm. The thickness of the thin InAs quantum well is not directly visible from the Kiessig fringe distances, but it becomes accessible via the phase contrast between the quantum well and the GaAs top layer. Assuming A_1 and A_3 are the amplitudes of the GaAs layers and t_2 the thickness of the InAs quantum well with $t_2 << (t_1 + t_3)$ the total scattering amplitude A is approximately given by[28]

$$A = A_1 + A_3 \exp\left[-i \frac{2\pi}{\lambda} \frac{2t_2}{\alpha_f}\right]. \quad (22)$$

The amplitude A_3 experiences a phase shift during the passage of the wave across the quantum well. It changes its magnitude and sign relative to A_1. Numerical simulation reveals that the angular position of the thickness oscillations depends on the effective thickness of the quantum well. In the present example the interfaces are not sharp. Instead the nominal thickness of one monolayer, the indium content is spread over about 5 mono-

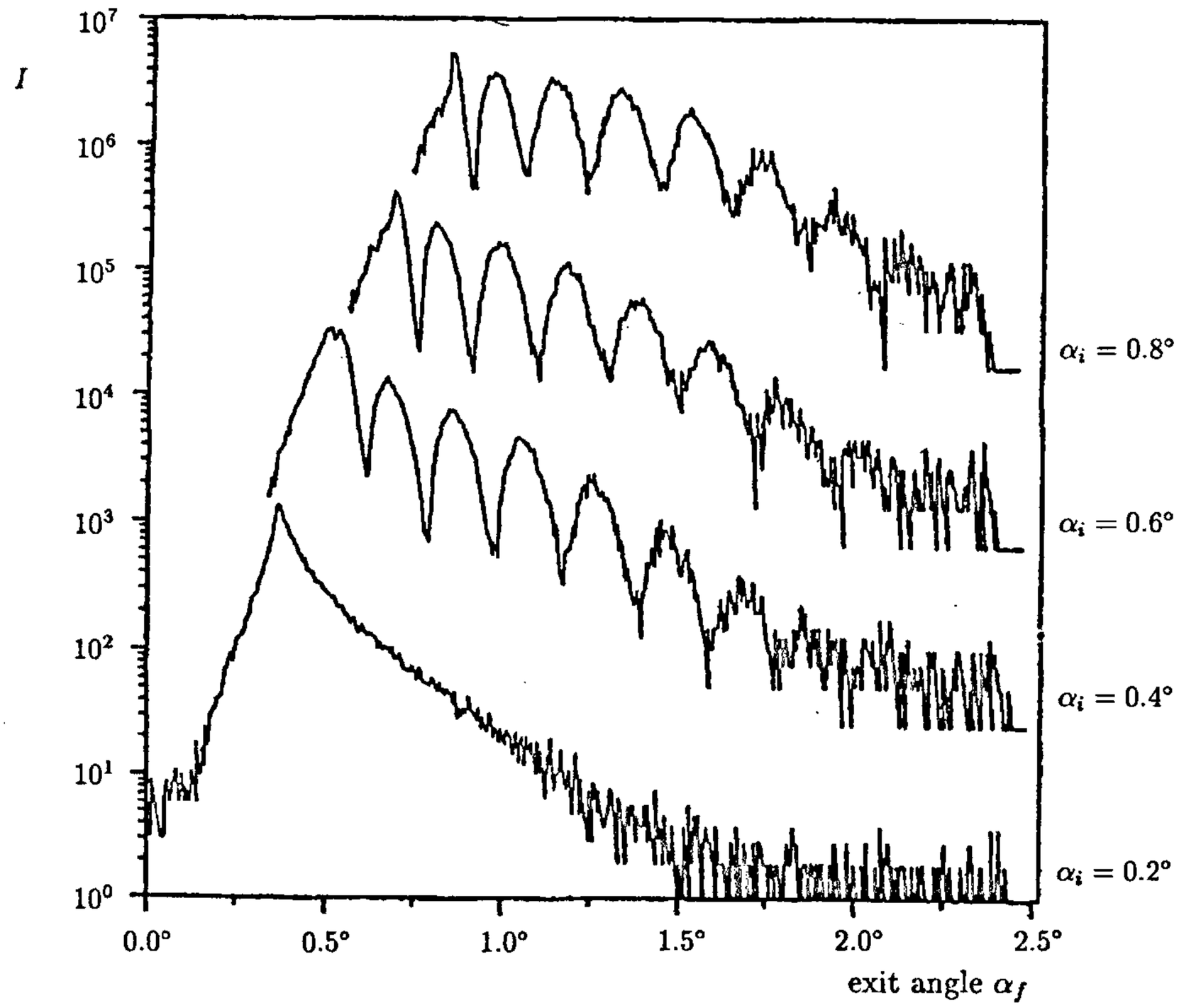

Figure 4. Scans of α_f at different values of α_i recorded in GID geometry for (200) in-plane diffraction from a GaAs/InAs/GaAs (001) single-quantum well structure.

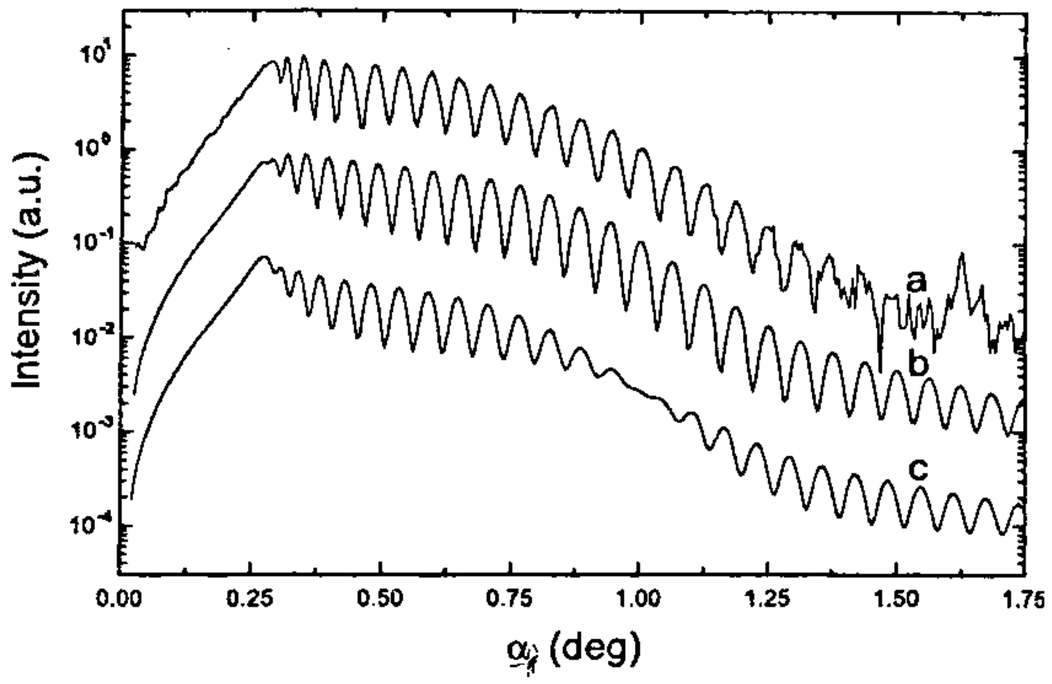

Figure 5. Experimental (curve a) and simulated q_z scans of a GaAs/$Ga_{0.87}In_{0.13}As$/GaAs (001) double heterostructure recorded under GID geometry close to the (200) in-plane GaAs reflection. The two simulations are of the expected rod structure, assuming abrupt interfaces (curve c) and a compositional grading close to a single interface (cuve b).

layers[29], which may be explained by lateral averaging of the scattering events across different monolayer steps.

Another example, shown in Figure 5, displays several α_f scans of a GaAs/$Ga_{0.87}In_{0.13}As$/GaAs double heterostructure with larger thicknesses compared to the previous example. The task here was to verify the existence of a compositional grading close to the GaAs–GaInAs interface which had been indicated by photoluminescence measurements[30]. The use of the (200) in-plane reflection was preferred for this purpose because it gives a large scattering contrast between the scattering amplitudes $\chi_{HGaInAs}$ and χ_{HGaAs}, which cannot be expected at the (400) diffraction. The angular spacing between the oscillations provides a top layer thickness $t = 112$ nm. Numerical simulation reveals that for sharp interfaces the truncation rod structure should show a modulation with a periodicity $\Delta\alpha_f = \lambda/t_{GaInAs}$ as follows from eq. (21); this is not visible in the experiment. The experimental curves can indeed be explained by considering the expected compositional grading. Unfortunately we are unable to tell whether the grading is close to the lower or the upper intrinsic interface. However, it amounts to one-fifth of the expected homogeneous thickness of the GaInAs layer[29].

Finally we give an example of the application of the GID technique for the characterization of multilayers. Figure 6 shows several α_f-resolved curves recorded from a MOCVD grown lattice matched GaInAs/InP superlattice[16]. For very low α_i no additional peak appears except that caused by the Fresnel function (see eq. (7)). Increasing the incidence angle, additional peaks appear measuring the superlattice spacing. From eq. (21) we obtain $t_{SL} = t_{GaInAs} + t_{InP} = 46$ nm. The thickness ratio

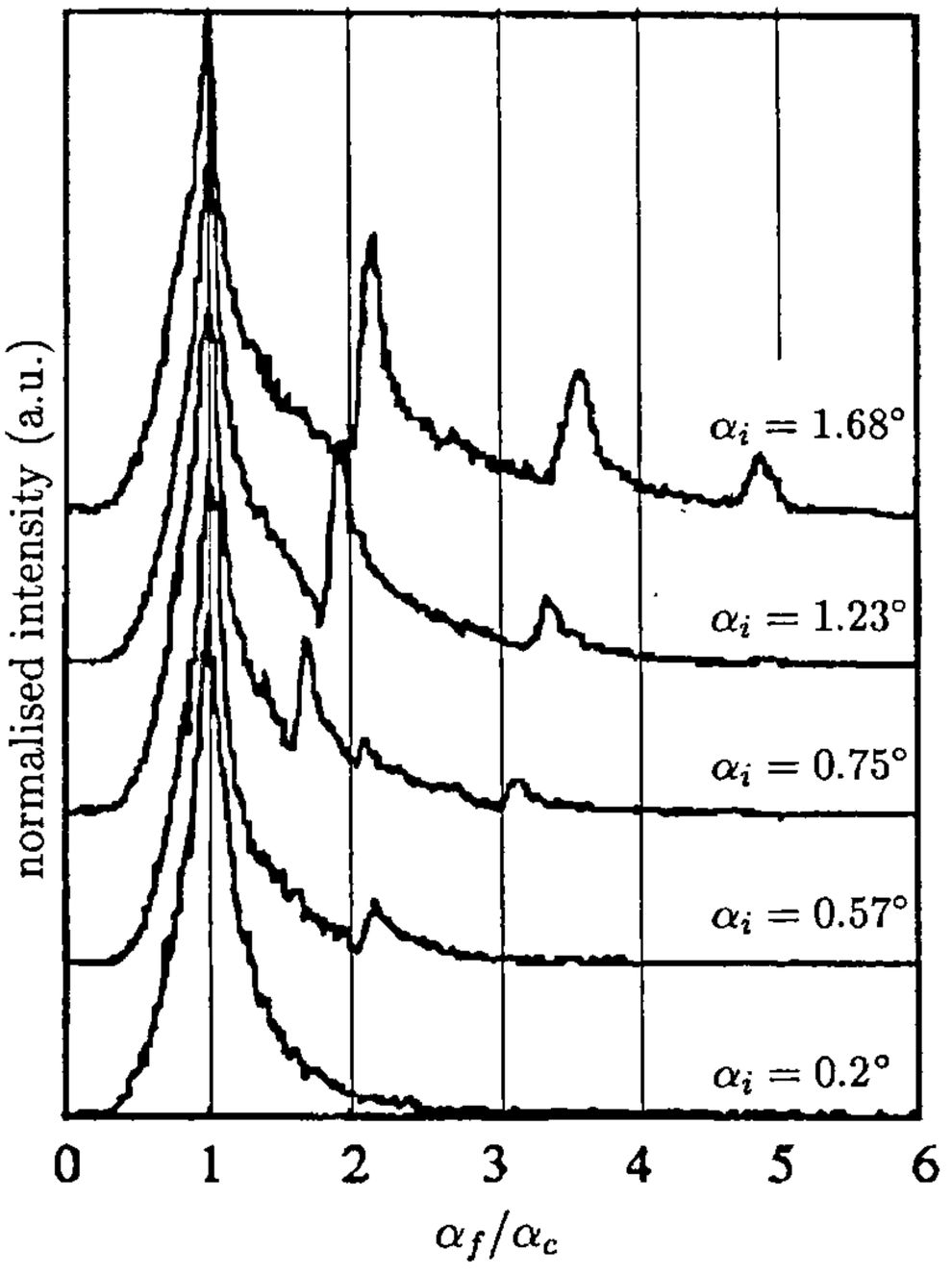

Figure 6. α_f-resolved GID intensities of an InGaAs/InP superlattic measured at the (220) Bragg position of InP at different α_i.

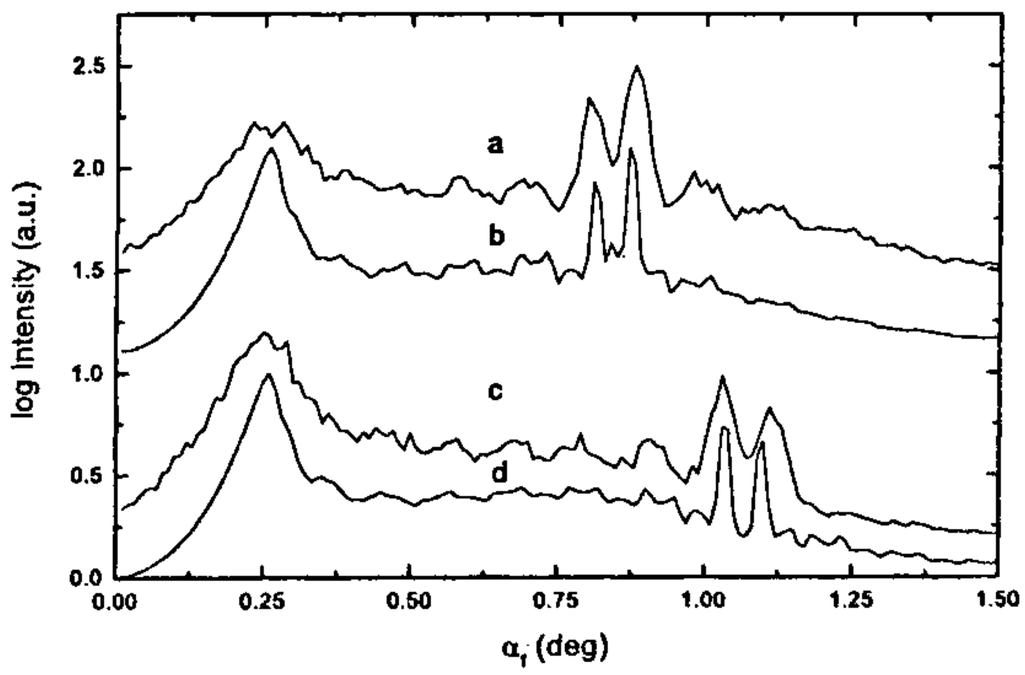

Figure 7. Measured (curves a and c) and calculated (curves b and d α_f scans of an InP/GaInAs multiplayer structure containing a buriec GaInAs enlarged quantum well. Curves a and b correspond tc $\alpha_i = 1.2°$, curves c and d to $\alpha_i = 1.4°$.

could not be determined due to the only moderate intensity of a bending magnet station at HASYLAB ($\lambda = 0.1388$ nm) used for this experiment. Because the electron density difference between both sublayers is about 7% there is a different critical angle of the top layer and the average superlattice. This appears as an asymmetry in the measured SL-peaks (see Figure 6).

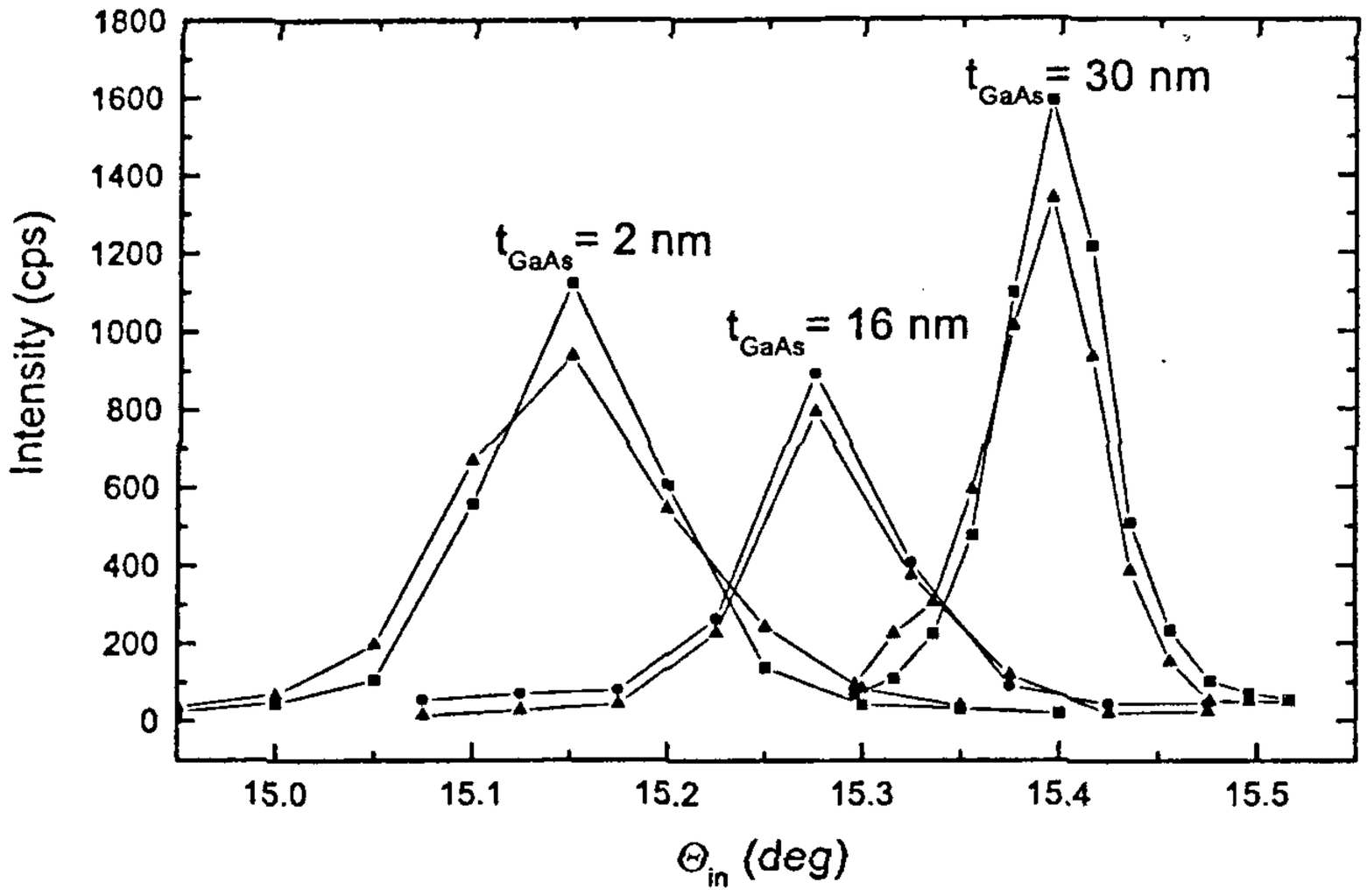

Figure 8. In-plane diffraction curves of several $Ga_{0.8}In_{0.2}As/GaAs$ multilayers with different thicknesses of the GaAs sublayers. The different in-plane peak positions indicate partial and complete relaxation.

The out-of-plane resolution was too poor to detect the thickness oscillations in the measured rod scans. Nevertheless, the total number of layers could be determined from the widths and the absolute intensity of the SL–Bragg peaks.

Figure 7 shows rod scans of a sample containing an enlarged GaInAs quantum well embedded between two superlattices each containing 15 InP/GaInAs periods with $t_{SL} = 9.4$ nm. Although the bad interface quality prevents the appearance of thickness fringes, the first-order superlattice peak is visible. Its double-peak behaviour is induced by the phase shift between the top and bottom superlattice after passing through the quantum well. It can be described by eq. (22) after the substitution of $A_{1,3}$ by the respective scattering amplitudes of both superlattices.

Thus the quantum well thickness is measured from the intensity ratio V between the two maxima at the first-order Bragg peak. V changes with α_i; we found $V < 1$ for $\alpha_i = 1.2°$ and $V > 1$ for $\alpha_i = 1.4°$. A fit of a computer simulation to the two curves gave the result $t_{GaInAs} = 5.26 \pm 0.24$ nm. This result has a relative precision better than 5% (ref. 31).

5.2. *Determination of lattice mismatches*

The GID scattering geometry enables a unique measurement of the in-plane lattice parameter even for very thin layers; this was the very first application of the GID scheme[6]. For semiconductor heterostructures, GID can be used to directly determine the degree of relaxation R in thin layers. R is defined by

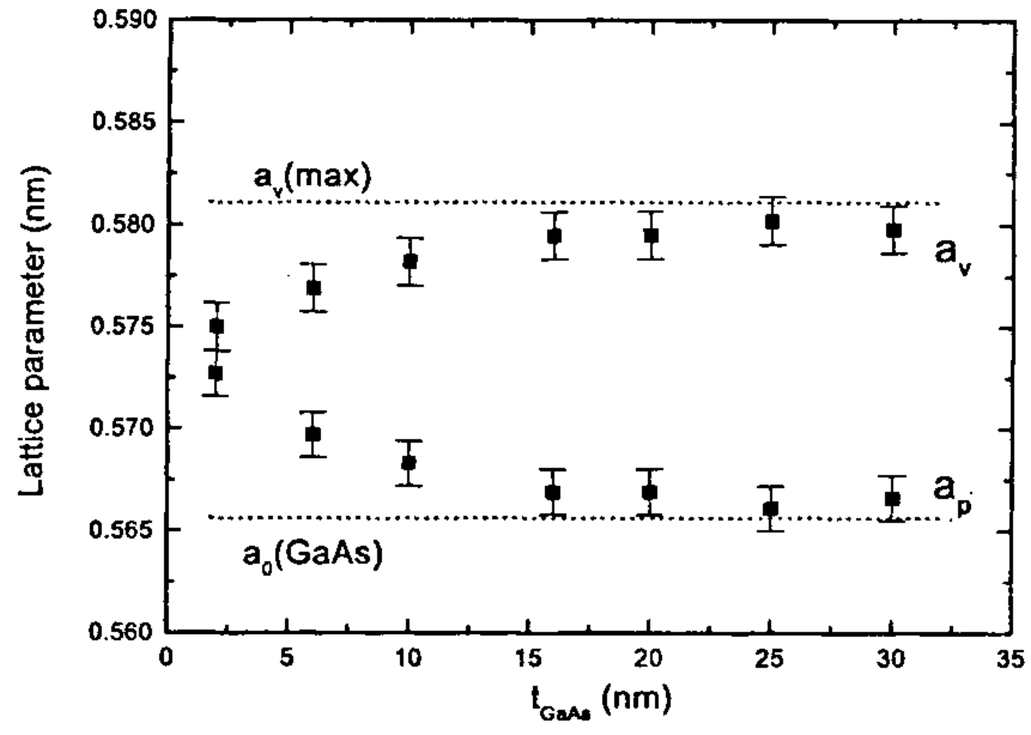

Figure 9. In-plane and out-of-plane lattice parameters of the GaInAs/GaAs multilayer system for which diffraction curves are shown in Figure 8.

$$R = \frac{a_{layer,\parallel} - a_{substrate}}{a_{layer} - a_{substrate}}, \tag{23}$$

where $a_{layer,\parallel}$ is the in-plane lattice parameter of the layer after growth onto the substrate and a_{layer} that of the free-standing material. $a_{substrate}$ is the lattice parameter of the substrate. An application is shown in Figure 8 for several $Ga_{0.8}In_{0.2}As/GaAs$ multilayers[32]. The samples have equal total thicknesses of the multiplayer ($t_{tot} = 800$ nm) and equal thicknesses of the $Ga_{0.8}In_{0.2}As$ sublayer ($t_{GaInAs} = 18$ nm), but they differ in the thickness of the GaAs spacers. Figure 8 shows the (200) in plane Bragg peak positions of the samples, measuring the average value of $a_{\parallel}$. For the sample with $t_{GaAs} = 30$ nm, the

measured diffraction maximum corresponds to the Bragg angle of the GaAs substrate. However, the multilayer Bragg angle decreases for decreasing t_{GaAs}, indicating the onset of relaxation of the multilayer. The evaluated values of R are confirmed by the out-of-plane lattice parameters measured by coplanar diffraction; it shows similar functional behaviour. R increases with decreasing t_{GaAs}. As shown in Figure 9, the multilayer system behaves approximately pseudomorphically for thick spacer layers ($t_{GaAs} = 30$ nm) but shows almost complete relaxation for $t < 2$ nm.

Figure 10 shows an example of a depth-resolved measurement of the in-plane lattice parameter from a multilayer composed by 60 periods of GaAs/$Ga_{1-x}In_xAs$ grown on GaAs [001] by MOVPE. From rod-scan measurements and using conventional X-ray diffraction the individual layer thicknesses were determined to be 12.1 nm and 2.9 nm, respectively. The sample was covered by a 100 nm-thick GaAs top layer. In order to determine the depth dependence of the lattice parameter various in-plane scans were recorded as a function of α_i. We used a position-sensitive detector aligned perpendicular to the sample surface. Applying the relaxed in-plane resolution of a bending-magnet station at BNL in Brookhaven, New York, the PSD records the whole intensity distribution towards q_z simultaneously for a fixed in-plane angle θ_B. The top curve (I_{tot}) in Figure 10 shows the α_f–integrated intensity at $\alpha_i \approx 2.5\alpha_c$ as a function of the angular deviation from the in-plane (200) Bragg diffraction of GaAs. The other curves show the corresponding intensities from selected channels of the PSD, i.e. integrated between $0 < \alpha_f < \alpha_c(I_1)$ ($\Lambda < 10$ nm) and $\alpha_c < \alpha_f < 2.5\alpha_c(I_2)$ ($\Lambda > 300$ nm). The two diffraction curves peak at different values of θ_B, indicating different in-plane lattice parameters in the top layer and within the multilayer. The value $a_{||}$ for the GaAs top layer (I_1) coincides with the lattice parameter of the substrate a_S, but the multilayer (I_2) is relaxed. The relaxation does not change abruptly at the interface between the top layer and the multilayer. The relaxation profile could be estimated via computer simulation from the GID curves measured at different values of α_i (ref. 24).

GID enables a very accurate determination of small in-plane lattice mismatches. This is realized by recording α_f scans instead of in-plane diffraction curves. If the thin top layer and the substrate differ in their in-plane lattice parameters, both of the corresponding reciprocal lattice points show separate truncation rods. These can be measured by a PSD as a function of α_f and θ_i. If the detector is fixed at the origin of the substrate truncation rod at $\sin\theta_{i1} = \lambda/2a_1$ and $\alpha_f \approx 0$ then for $a_1 < a_2$ the PSD cuts the other truncation rod, corresponding to a_2, at the position $\sin\theta_{i2} = \lambda/2a_2$ and $\alpha_f > 0$ (ref. 33). This situation is expressed by

$$\Delta\alpha_f^2 = \alpha_i^2 \cos(2\theta_B) - 2(\Theta_{i1} - \Theta_{i2})\sin(2\Theta_B). \quad (24)$$

If both α_i and α_f are small, a very small angular separation $\Theta_{i1} - \Theta_{i2}$ becomes expanded towards the α_f axis. For $\alpha_i \approx \alpha_c$ and $\Theta_B \approx 15°$, the stretching factor is of the order of 100.

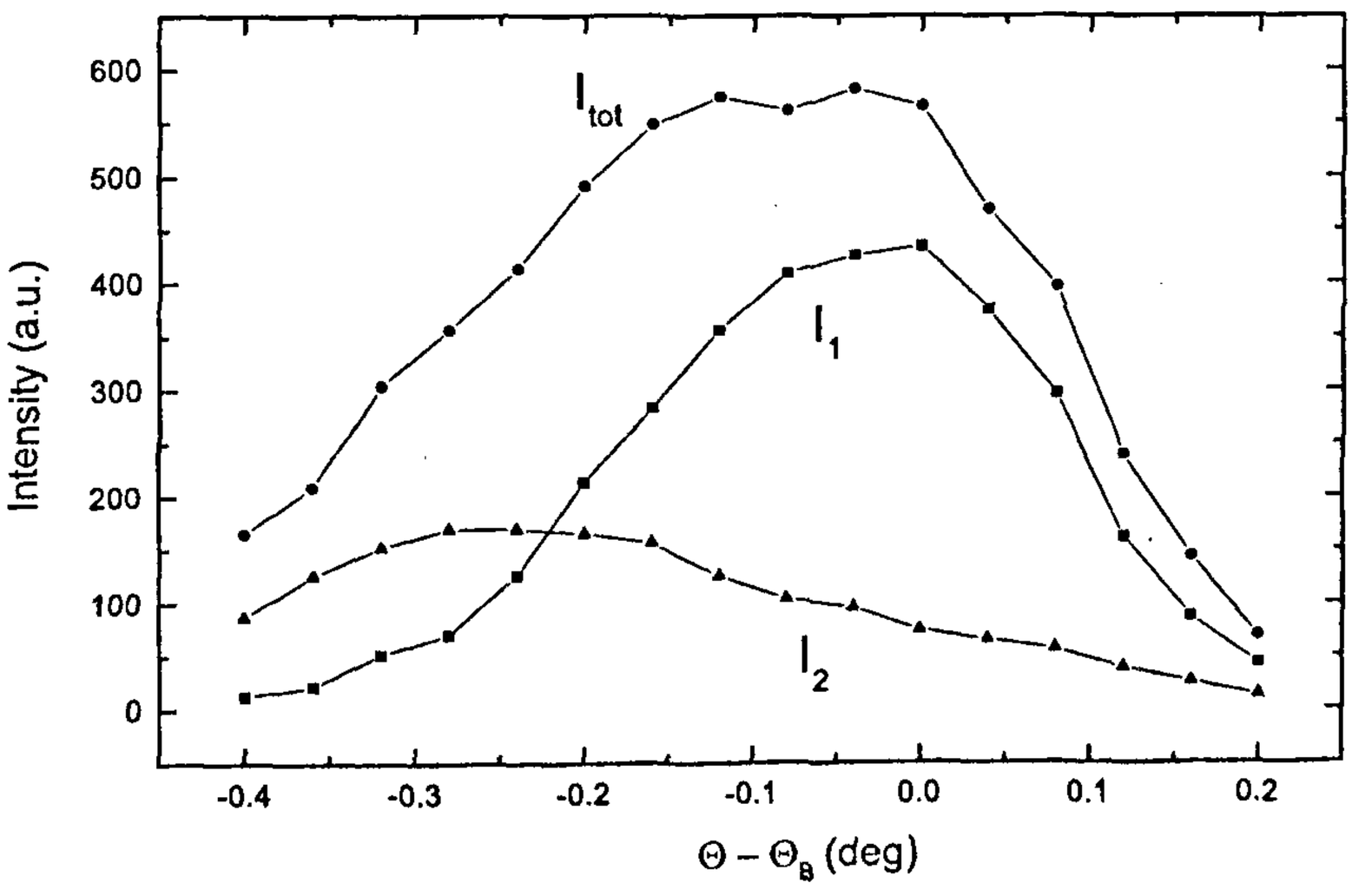

Figure 10. Depth-resolved evaluation of in-plane lattice parameters of a GaInAs/GaAs multilayer system (I_2) covered by a 100 nm thick GaAs top layer (I_1). I_{tot} is the measured curve without α_f resolution.

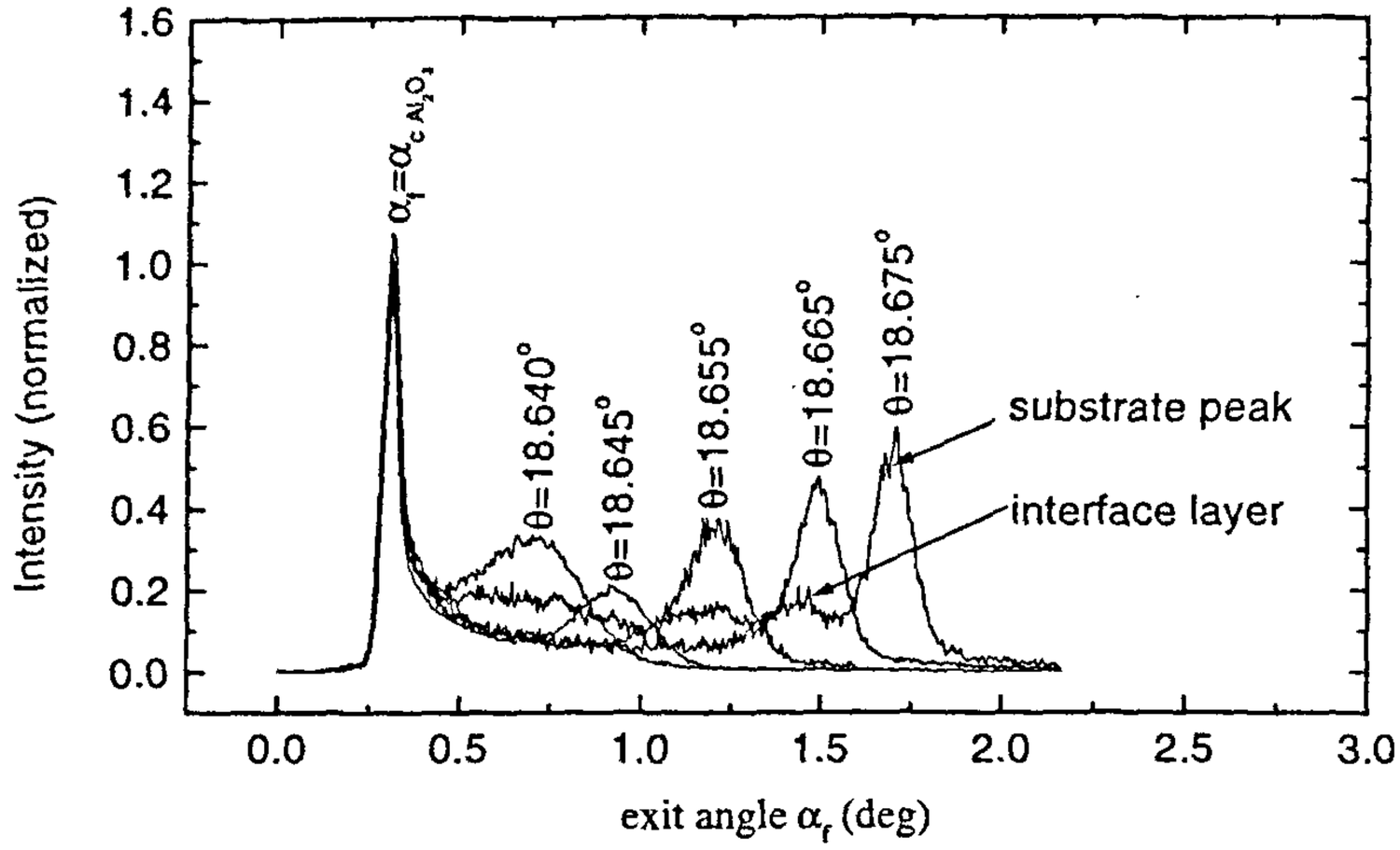

Figure 11. α_f-resolved Bragg intensity of a silicon layer on sapphire. The lattice mismatch is obtained after extrapolation to $\alpha_f = 0$.

Figure 11 shows several α_f scans of a thin silicon layer sputtered on sapphire, recorded at different in-plane positions Θ_i. Both the substrate peak and an interface peak can be clearly distinguished. The peak on the left always marks the critical angle α_c of the sapphire substrate; the silicon layer peak is not visible. The other two peaks change on the α_f scale when the onset angle of the PSD is changed by Θ_i. The corresponding lattice parameters are obtained by extrapolating the respective α_f positions of the two peaks to $\alpha_f = 0$. Both peaks are separated by $\Delta a_{\parallel}/a = 8 \times 10^{-4}$. The presence of the interface peak is explained by a very thin aluminium silicate layer which is formed during the growth of the silicon layer by diffusion of aluminium out of the sapphire substrate.

5.3. *Investigation of surface nanostructures*

The GID technique possesses a great potential for the characterization of surface–patterned structures by virtue of its surface sensitivity. If the spacing of the lateral grating is of the order of several 100 nm, the experiment needs good in-plane resolution in order to separate the grating side peaks. This is performed by attaching an analyser crystal in front of the detector (see Figure 3). Because the intensity of the grating side peaks are several orders of magnitude lower compared with any fundamental Bragg diffraction, the experiment requires the use of a wiggler or undulator beamline of a synchrotron facility. Our experiments have been performed mainly at the BW2 station at HASYLAB.

One problem in the characterization of surface gratings is the separation of the effect of strain and grating shape in the X-ray diffraction curve. For cubic substrates and surface wires there is a unique possibility for such a separation[34]. Assuming a [001] surface and an alignment of the wires in the [110] direction, grating truncation rods appear in addition to the rod of the substrate and are aligned in [110] as well. Running an in-plane scan close to the (220) diffraction, the grating peaks appear upon rotating the sample across a fixed detector position. This *transversal scan* or *ω-scan* keeps the length of the reciprocal space vector constant and thus it is insensitive to strain. All scans performed in this manner contain unique information about the shape of the grating. On the other hand, scanning the (220) diffraction, the grating peaks become visible only by changing the length of the reciprocal space vector. This *longitudinal scan* or *ω*:2*θ-scan* measures both strain and shape.

Figure 12 shows transversal scans of three GaAs surface gratings with $D = 250$ nm but varied width of the wires. All scans look very symmetric with respect to the GaAs Bragg peak marked by $\Delta q_x = 0$. At selected angular positions of grating peaks of sample A we performed rod-scans, shown in Figure 13. The intensity modulation along θ_z measures the etching depth of the grating; here it is about 27 nm. The oscillation maximum of the various rod scans are shifted against each other. This phase shift reflects the trapezoidal shape of the wires. In the present case, the inclination of side planes is close to [111]. Figure 14 displays several longitudinal scans of sample A recorded at different α_i. Even for larger penetration depths, it looks no more symmetrical due to the influence of lattice relaxation induced by a 4.4 nm thick $In_{0.14}Ga_{0.86}As$ quantum well embedded within the wires at about 15 nm below the wire surface. Induced by the

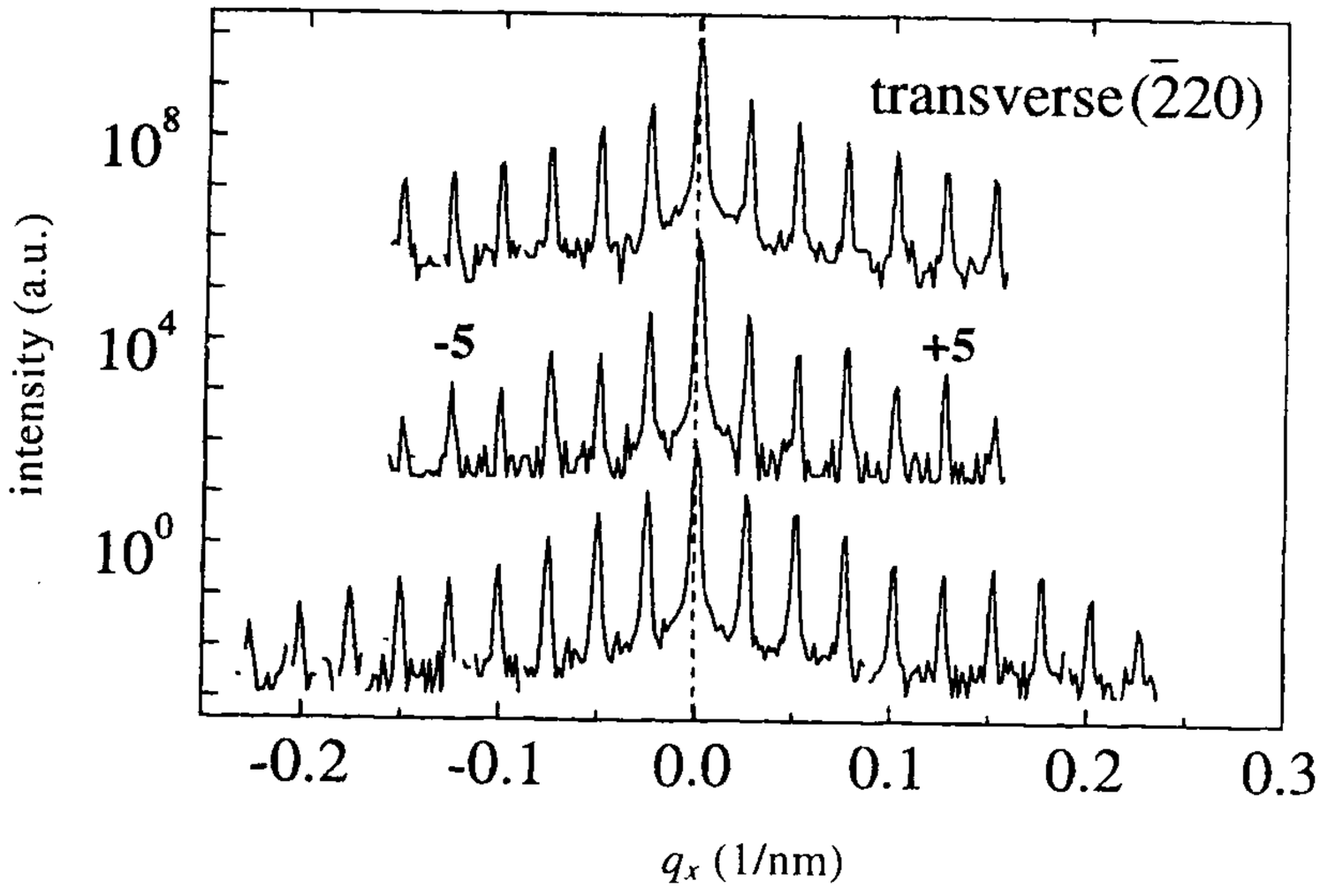

Figure 12. Transverse scans recorded across the (2$\bar{2}$0) diffraction of three surface nanostructures with different wire widths.

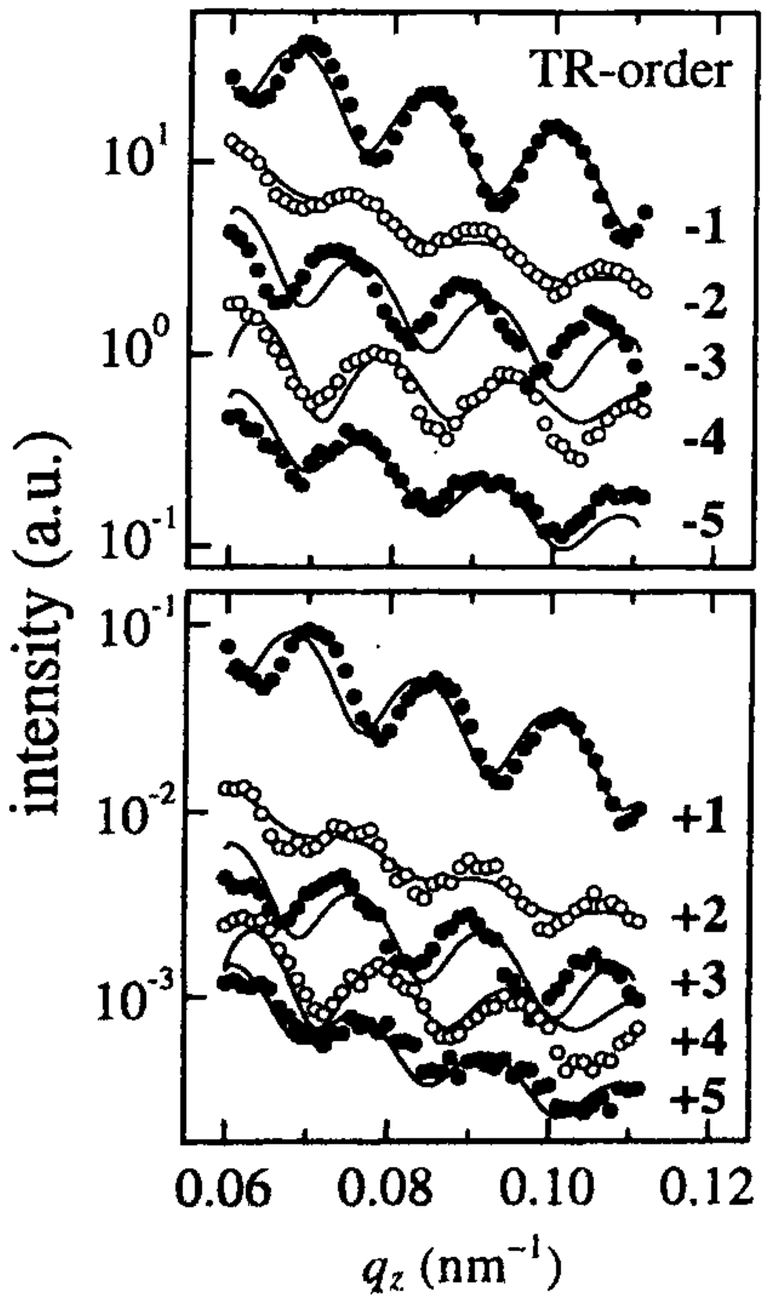

Figure 13. Grating rod intensities recorded at selected peaks of the transverse scan of sample A shown in Figure 12.

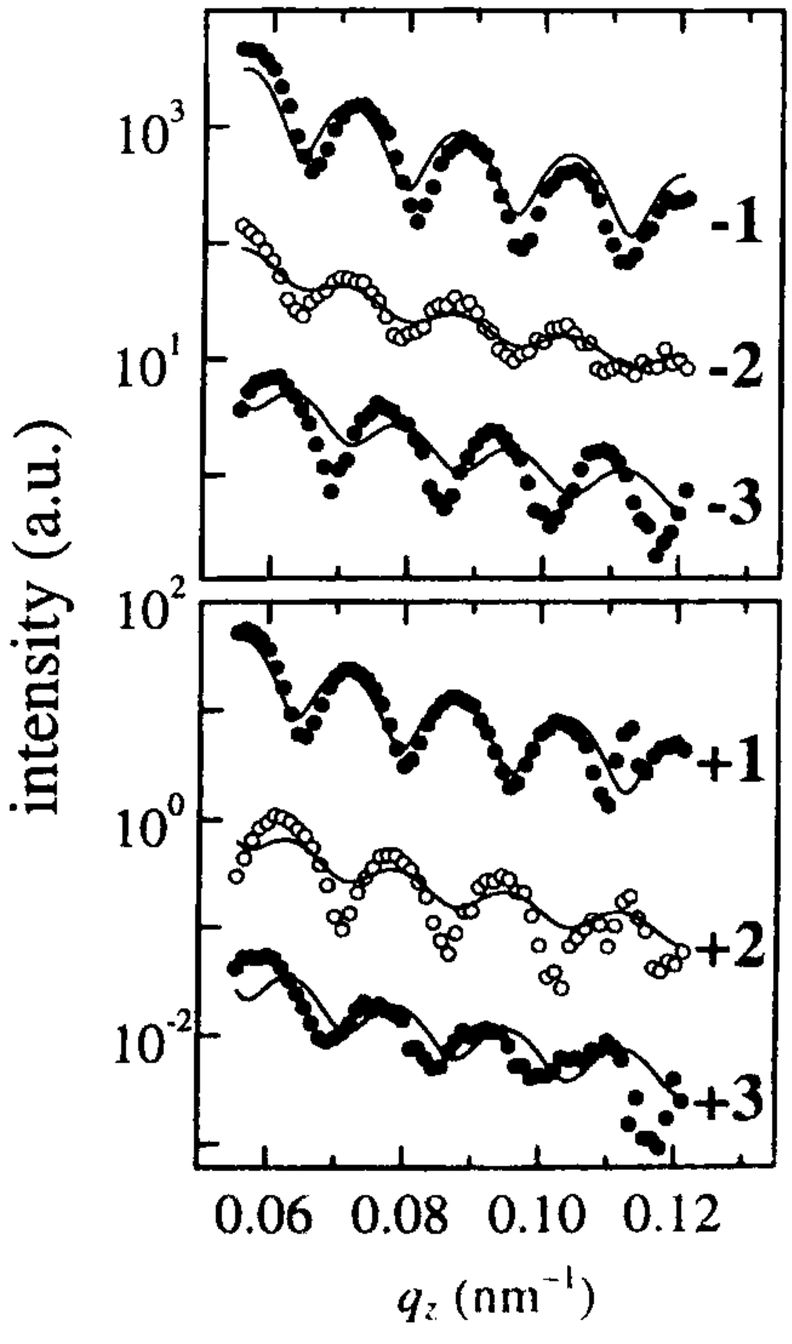

Figure 14. Longitudinal scans across the (2$\bar{2}$0) diffraction of sample A recorded at different penetration depths.

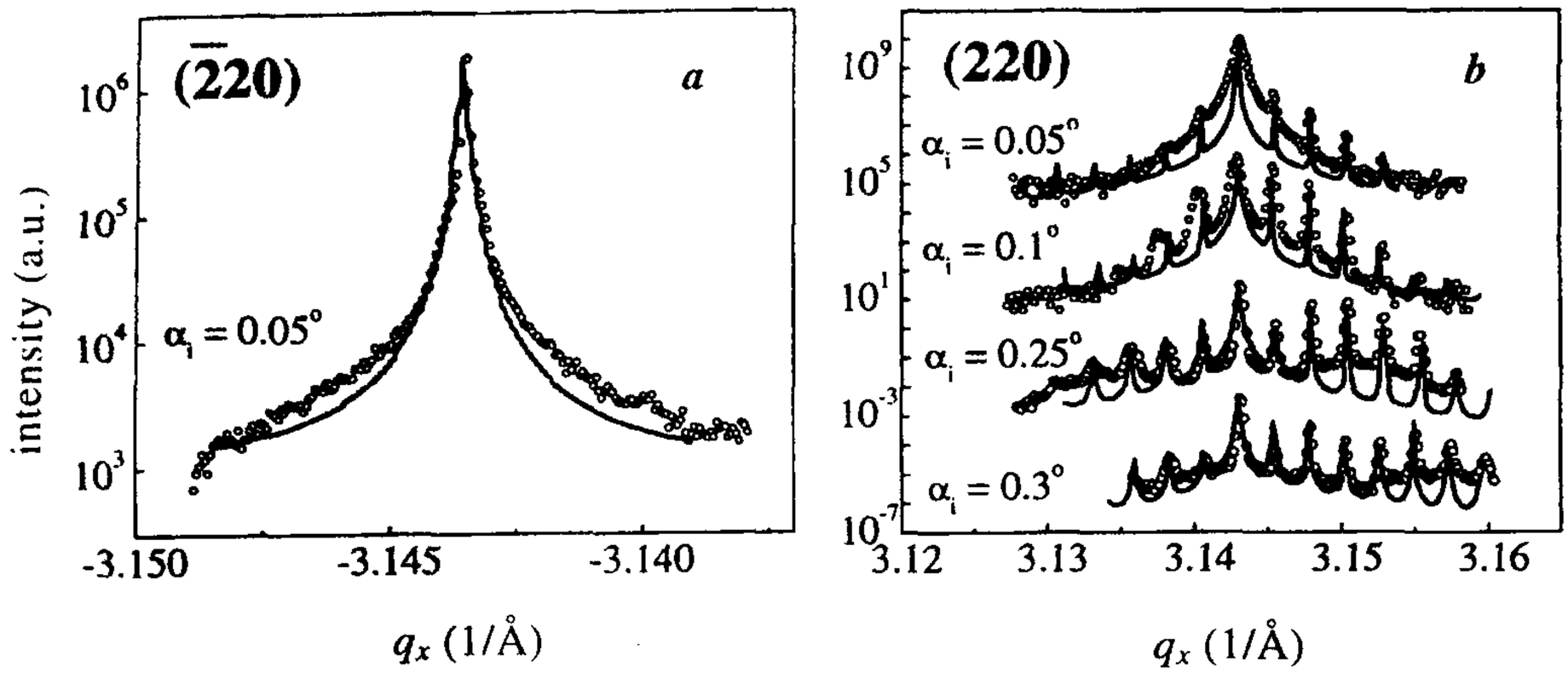

Figure 15. *a*, Strain insensitive transverse and *b*, strain sensitive longitudinal at different α_i, scans of a surface wire structure covered by an additional MBE step.

process of etching, the pseudomorphic constraint loosens and the lattice becomes slightly relaxed near the quantum well. The relaxation corresponds to a lateral mismatch of $\Delta a_{\parallel}/a \approx 3 \times 10^{-4}$ (ref. 35).

The fitting of the curves has been performed in terms of a semi-kinematic approach of the DWBA developed by Baumbach and Gailhanou[36] for multilayer gratings. Qualitatively it contains similar relations as shown in eq. (16). Meanwhile, this approach is well adapted for GID experiments[37].

Finally we will show that GID is most meaningful for the characterization of buried surface gratings. For reasons of improving the photoluminescence yield, artificial surface nanostructures are overgrown by a material with a nearly similar lattice parameter as the substrate. After the overgrowth, the sample surface is completely smooth. Verified by AFM inspection, no periodic modulations remain. Nevertheless, the buried surface grating induces the formation of a periodic strain modulation within the overlayer which can be identified by using X-ray methods[38,39]. Figure 15 shows a transverse and several longitudinal scans of a similar grating structure discussed earlier after a MBE overgrowth with about 40 nm of GaAs. Whereas the longitudinal scan displays remarkable grating peaks which change their intensity when changing Λ, the transverse scan does not exhibit such grating peaks. Both sets of curves can be understood by the disappearance of the density modulation but existence of a strain modulation within the overlayer as mentioned earlier. In the present case the X-ray data were used to adapt the parameters of a model structure compiled in terms of a finite element calculation of the 3D strain distribution in such structures. The fit results were used to interpret the strain-induced shift of the PL energy of similar samples[37].

It should be noted that very recently GID measurements have been made on artificially structurized[40] as well as self-organized[41–43] quantum dot arrays. A detailed discussion of these experiments is out of the scope of this article.

1. Beenakker, C. W. J. and van Houten, H., in *Solid State Physics*, Academic Press, Boston, 1991, vol. 44.
2. Bimberg, D., Grundmann, M. and Ledentsov, N. N., *Quantum Dot Heterostructures*, John Wiley & Sons, Chichester, 1999.
3. Holy, V., Pietsch, U. and Baumbach, T., *Springer Tracts in Modern Physics*, 1999, vol. 149, Berlin.
4. Pietsch, U. and Borchard, W., *J. Appl. Crystallogr.*, 1987, **20**, 8–10.
5. Gerhard, T., Faschinger, W. and Landwehr, G., *J. Phys. D., Appl. Phys.*, 1999, **32**, 583–589.
6. Marra, W. C., Eisenberger, P. and Cho, A. Y., *J. Appl. Phys.*, 1979, **50**, 6927–6933.
7. Vineyard, G. D., *Phys. Rev. B*, 1982, **26**, 4146–4159.
8. Dosch, H., Battermann, B. and Wuck, D. C., *Phys. Rev. Lett.*, 1986, **56**, 1144–1147.
9. Sinha, S. K., Sirota, E. B., Garoff, S. and Stanley, H. B., *Phys. Rev. B*, 1988, **38**, 2297–2311.
10. Dosch, H., in *Springer Tracts in Modern Physics*, 1992, vol. 126, Berlin.
11. Bernhard, N., Burkel, E., Gompper, G., Metzger, H. and Peisl, J., *Z. Phys. B (Condens Matter)*, 1987, **69**, 303–311.
12. Rugel, S., Metzger, H., Wallner, G. and Peisl, J., *Appl. Surf. Sci.*, 1991, **54**, 507–510.
13. Afanasev, A. M. and Melkonyan, O. G., *Acta Crystallogr. A*, 1983, **39**, 207–210.
14. Golovin, A. L. and Imamov, R. M., *Phys. Status Solidi A*, 1983, **80**, K63–K65.
15. Aleksandrov, P. A., Afanasiev, A. M. and Stepanov, S. A., *Phys. Status Solidi A*, 1984, **86**, 143–154.
16. Pietsch, U., Seifert, W., Fornell, J. O., Rhan, H., Metzger, H., Rugel, S. and Peisl, J., *Appl. Surf. Sci.*, 1992, **54**, 502–506.
17. Feidenhans'l, R., *Surf. Sci. Rep.*, 1989, **10**, 125
18. Rhan, H. and Peisl, J., *Z. Phys. B (Condens Matter)*, 1996, **100**, 365–368.

19. Stepanov, S. A., Kondrashkina, E. A., Köhler, R., Novikov, D. A., Materlik, G. and Durbin, S. M., *Phys. Rev. B*, 1998, **57**, 4829–4841.
20. Rhan, H. and Pietsch, U., *Z. Phys. B* (*Condens Matter*), 1990, **80**, 347–352.
21. Stepanov, S. A., Pietsch, U. and Baumbach, G. T., *Z. Phys. B (Condens Matter)*, 1995, **96**, 341–347.
22. http://sergey.bio.aps.anl.gov.
23. Ulyanenkov, A. P., Stepanov, S. A., Pietsch, U. and Köhler, R., *J. Phys. D. Appl. Phys.*, 1995, **28**, 2522–2528.
24. Pietsch, U., Metzger, T. H., Rugel, S., Jenichen, B. and Robinson, I. K., *J. Appl. Phys.*, 1993, **74**, 2381–2387.
25. Darowski, N., Paschke, K., Pietsch, U., Wang, K.-H., Forchel, A., Baumbach, T. and Zeimer, U., *J. Phys. D, Appl. Phys.*, 1997, **30**, L55–L59.
26. Shen, Q., Kycia, S. W., Tentarelli, E. S., Schaff, W. J. and Eastman, L. F., *Phys. Rev. B*, 1996, **54**, 16381–16384.
27. Bahr, D., Press, W., Jebasinski, R. and Mantl, S., *Phys. Rev. B*, 1995, **51**, 12223–12238.
28. Baumbach, G. T., Rhan, H. and Pietsch, U., *Phys. Status Solidi A*, 1988, **109**, K7–K11.
29. Rose, D., Pietsch, U. and Zeimer, U., *J. Appl. Phys.*, 1997, **81**, 2601–2606.
30. Zeimer, U. PhD, Thesis, University of Potsdam, 1998.
31. Pietsch, U., Metzger, T. H. and Seifert, W., *J. Appl. Phys.*, 1995, **78**, 3144–3148.
32. Rose, D., Pietsch, U., Förster, A. and Metzger, H., *Physica B*, 1994, **198**, 256–258.
33. Metzger, T. H., Pietsch, U., Garstein, E. and Peisl, J., *Phys. Status Solidi A*, 1999, **174**, 403–411.
34. Darowski, N., Paschke, K., Pietsch, U., Wang, K., Forchel, A., Lübbert, D. and Baumbach T., *Physica B*, 1998, **248**, 104–108.
35. Ulyanenkov, A., Baumbach, T., Darowski, N., Pietsch, U., Wang, K.-H., Forchel, A. and Wiebach, T., *J. Appl. Phys.*, 1999, **85**, 1524–1530.
36. Baumbach, T. and Gailhanou, M., *J. Phys. D*, 1995, **28**, 2321–2327.
37. Ulyanankov, A., Darowski, N., Grenzer, J., Pietsch, U., Wang, K. H. and Forchel, A., *Phys. Rev. B*, 1999, **60**, 16701–16714.
38. Darowski, N., Pietsch, U., Zeimer, U., Smirnitzki, V. and Bugge, F., *J. Appl. Phys.*, 1998, **84**, 1366–1370.
39. Lübbert, D., Baumbach, T., Ponti, S., Pietsch, U., Leprince, L., Schneck, J. and Talneau, A., *Europhys. Lett.*, 1999, **46**, 479–485.
40. Darowski, N., Pietsch, U., Zhuang, Y., Zerlauth, S., Bauer, G., Lübbert, D. and Baumbach, T., *Appl. Phys. Lett.*, 1998, **73**, 806–808.
41. Holy, V., Darhuber, A. A., Stangl, J., Zerlauth, S., Schäffler, F., Bauer, G., Darowski, N., Lübbert, D., Pietsch, U. and Vavra, I., *Phys. Rev. B*, 1998, **58**, 7934–7943.
42. Kegel, I., Metzger, T. H., Peisl, J., Schittnhelm, P. and Abstreiter, G., *Appl. Phys. Lett.*, 1999, **74**, 2978–2980.
43. Stangl, J., Holy, V., Mikulik, P., Bauer, G., Kegel, I., Metzger, T. H., Schmidt, O. G., Lange, C. and Eberl, K., *Appl. Phys. Lett.*, 1999, **74**, 3785–3787.

ACKNOWLEDGEMENTS. This work was supported by the BMBF (grant 05 5IPAAI) and the VW foundation (grant I70/588). I thank Dirk Rose, Nora Darowski, Thomas Geue and Jörg Grenzer for their work at the University of Potsdam and T. H. Metzger (Uni München), T. Baumbach (FHI Saarbrücken), Alex Ulyanankov (Rigaku Corp, Tokyo) for the fruitful collaboration.